Magic wavelengths for the helium $2\,^3S_1 \rightarrow 2\,^1P_1$ forbidden transition

Yong-Hui Zhang, Li-Yan Tang, Jun-Yi Zhang, and Ting-Yun Shi[*]

State Key Laboratory of Magnetic Resonance and Atomic and Molecular Physics, Wuhan Institute of Physics and Mathematics, Innovation Academy for Precision Measurement Science and Technology, Chinese Academy of Sciences, Wuhan 430071, People's Republic of China

A series of magic wavelengths for the forbidden transition of $2\,^3S_1 \rightarrow 2\,^1P_1$ in helium are determined by performing large-scale full relativistic configuration interaction calculations based on Dirac-Coulomb-Breit Hamiltonian with the mass shift operator included. QED corrections to magic wavelengths are taken into account by using the perturbation theory in nonrelativistic configuration interaction calculations. The 1335.55(2)-nm magic wavelength for the $2\,^3S_1(M = \pm 1) \rightarrow 2\,^1P_1(M = 0)$ transition is found to be sensitive to the finite nuclear mass, relativistic, and QED effects, and its measurement might provide a test of atomic structure theory.

I. INTRODUCTION

Quantum electrodynamics (QED) theory has developed to be one of the most successful theories in modern physics, since the Lamb shift between the $2s_{1/2}$ and $2p_{1/2}$ energy levels of hydrogen was discovered by Lamb and Retherford [1]. The measurement of the magnetic moment of the electron bound in hydrogenlike $^{12}C^{5+}$ ion yields the atomic mass of the electron with a relative precision of 3×10^{-11}, which represents one of the stringent tests of QED theory [2,3]. However, there are still unknown factors and parameters, such as the proton radius (r_p) puzzle of the surprising discrepancy between results from different methods for measuring the proton charge radius. In particular, the latest electron-based measurement of r_p agrees with the muonic hydrogen measurement but disagrees with the averaging of previous electron-based measurements [4], which calls for an imperative to test QED with other systems.

The well-established field of precision spectroscopy in helium (see Refs. [5–7] and references therein) has made many foundational contributions to accurate tests of QED theory. The increasingly improved measurements of the ground-state Lamb shift provide rigorously tests of bound-state QED in two-electron systems [8–10]. The presently most accurately known transition frequencies between the $2\,^3P_J$ levels [11–13] combined with the rigorous nonrelativistic QED (NRQED) calculations [14] determine the fine structure constant with an accuracy of several ppb. There are significant inconsistencies for the nuclear charge radius attained from different transitions of $2\,^3S \rightarrow 2\,^3P$ [15–17] and $2\,^3S_1 \rightarrow 2\,^1S_1$ [18–20]. Recently, a significant theoretical advance in the Lamb shift of helium has been achieved, which will allow comparison of the nuclear radius determined from the electronic and muonic helium and thus provides insight into the validity and limitations of QED theory [21].

In addition, unlike the precision spectral measurements, measurements of transition rates also can provide tests of

QED theory. The Einstein A coefficient for the $2\,^3S_1 \rightarrow 3\,^3S_1$ in helium is newly measured, which is compared to the theoretical value [22], leading to tests of both QED contributions and different QED frameworks. There are other means of measuring transition rate information in helium in order to test QED, such as static dipole polarizability in the ground state, for which the current comparison between experiment and theory has reached a level of ppm [23,24]. QED correction to static dipole polarizability of the $2\,^3S_1$ state in helium reaches 22.5 ppm, which may enable a new QED test [25]. However, measurements of atomic polarizabilities are somewhat rarer than calculations, and it is difficult to further improve measurement precision.

There is another nonenergy QED test that uses the tune-out wavelength. Since the measurement of a tune-out wavelength is a null experiment, and there is no need to know the intensity and beam profile of the irradiating laser precisely, the measurement of tune-out wavelengths can potential achieve high precision. Using the 413-nm tune-out wavelength of the $2\,^3S_1$ state in helium to probe atomic structure theory was proposed by Mitroy and Tang [26]. In followup works, high-accuracy calculations [25,27] and precision measurement [28] of the 413-nm tune-out wavelength reach a consistency on the order of ppm. The constantly advancing measurements and calculations are expected to determine this tune-out wavelength with a relative uncertainty of less than ppm.

Similarly, the measurement of a magic wavelength, at which the frequency-dependent polarizabilities of the initial and final states of a transition are equal, can be also very accurate. For example, the magic frequency for Sr optical clock transition has recently been measured with a fractional uncertainty of several ppb [29]. Magic wavelengths are widely used in state-of-the-art optical transition atomic clocks [30]. Besides that, magic wavelengths of helium would be sensitive to relativistic and QED effects. It would be worthwhile to determine magic wavelengths that would be the best atomic structure theory probes [26].

In this work, we will identify magic wavelengths that might be measured and provide a QED test. *B*-spline relativistic

---
*tyshi@wipm.ac.cn

configuration interaction (RCI) calculations are carried out to obtain the dynamic dipole polarizabilities for the $2\,^1P_1$ state of helium, which include the finite nuclear mass and relativistic corrections. Combined with our previous dynamic dipole polarizabilities of the $2\,^3S_1$ state [25], a series of magic wavelengths for the $2\,^3S_1 \rightarrow 2\,^1P_1$ transition are determined. QED effects on the static dipole polarizability for the $2\,^1P_1$ state, and on the 1335-nm magic wavelength for the $2\,^3S_1 \rightarrow 2\,^1P_1$ transition are evaluated as well by using the perturbation theory in nonrelativistic configuration interaction (NRCI) calculations. Atomic units (a.u.) are used throughout this paper unless stated otherwise.

II. METHOD

The RCI calculations are performed to solve the eigenvalue problem of the following Dirac-Coulomb-Breit (DCB) Hamiltonian with mass shift (MS) operator,

$$
\begin{aligned}
H = \sum_{i=1}^{2} & \left[c\boldsymbol{\alpha}_i \cdot \boldsymbol{p}_i + \beta m_e c^2 - \frac{Z}{r_i} \right] + \frac{1}{r_{12}} - \frac{1}{2r_{12}}[\boldsymbol{\alpha}_1 \cdot \boldsymbol{\alpha}_2 \\
& + (\boldsymbol{\alpha}_1 \cdot \hat{\boldsymbol{r}}_{12})(\boldsymbol{\alpha}_2 \cdot \hat{\boldsymbol{r}}_{12})] \\
& + \frac{1}{2m_0} \sum_{i,j}^{2} \boldsymbol{p}_i \cdot \boldsymbol{p}_j - \frac{1}{2m_0} \sum_{i,j}^{2} \frac{\alpha Z}{r_i} \left[\boldsymbol{\alpha}_i + \frac{(\boldsymbol{\alpha}_i \cdot \boldsymbol{r}_i)\boldsymbol{r}_i}{r_i^2} \right] \cdot \boldsymbol{p}_j,
\end{aligned}
\tag{1}
$$

where $c = 137.035\,999\,074$ is the speed of light [31], $\boldsymbol{\alpha}_i$ and β are the 4×4 Dirac matrices, $\boldsymbol{p}_i$ is the momentum operator for the ith electron, $m_e = 1$ is the electron mass, Z is the nuclear charge, r_i represents the distance of the ith electron from the nucleus, $\hat{\boldsymbol{r}}_{12}$ is the unit vector of the electron-electron distance $\boldsymbol{r}_{12}$, $m_0 = 7294.299\,5361\,m_e$ [31] is the nuclear mass of ^{4}He, $\alpha = 1/c$ is the fine-structure constant, the MS operator includes the nonrelativistic and leading relativistic components [25,32], and the leading relativistic correction to the mass shift with Dirac wave functions has been formulated in Refs. [33,34].

The eigenfunction $\psi_{ij}(JM)$ of an atomic state with angular momentum (J, M) is expanded as a linear combination of two-electron configuration-state functions $\phi_{ij}(JM)$,

$$
|\phi_{ij}(JM)\rangle = \eta_{ij} \sum_{m_i m_j} \langle j_i m_i; j_j m_j | JM \rangle a^{\dagger}_{im_i} a^{\dagger}_{jm_j} |0\rangle,
\tag{2}
$$

which are constructed by the single-electron wave functions, i.e., $a^{\dagger}_{im_i}|0\rangle$ and $a^{\dagger}_{jm_j}|0\rangle$, with the orbital angular momentums

ℓ_i and ℓ_j less than the maximum number of partial wave $\ell_{\max}$. η_{ij} is a normalization constant, $\langle j_i m_i; j_j m_j | JM \rangle$ represents the Clebsch-Gordan coefficient of jj coupling, $a^{\dagger}_{im_i}$ and $a^{\dagger}_{jm_j}$ are called creation operators, and $|0\rangle$ is the vacuum state. The ith single-electron wave function $a^{\dagger}_{im_i}|0\rangle$ is acquired by solving the single-electron Dirac equation using the Notre Dame basis sets of N number of B-spline functions with order of $k = 7$ [35,36].

Magic wavelengths are located by calculating the frequency-dependent polarizabilities of two states involved in the atomic transition and finding their crossing points. The dynamic dipole polarizability of the magnetic sublevel $|N_g J_g M_g\rangle$ under the linearly polarized light with laser frequency ω is expressed as [37]

$$
\alpha_1(\omega) = \alpha_1^S(\omega) + \frac{3M_g^2 - J_g(J_g+1)}{J_g(2J_g-1)} \alpha_1^T(\omega),
\tag{3}
$$

where $\alpha_1^S(\omega)$ and $\alpha_1^T(\omega)$ are the scalar and tensor dipole polarizabilities, which are respectively given by

$$
\alpha_1^S(\omega) = \sum_{n \neq g} \frac{f_{gn}^{(1)}}{(\Delta E_{gn})^2 - \omega^2}
\tag{4}
$$

and

$$
\begin{aligned}
\alpha_1^T(\omega) = \sum_{n \neq g} (-1)^{J_g + J_n} & \sqrt{\frac{30(2J_g+1)J_g(2J_g-1)}{(2J_g+3)(J_g+1)}} \\
& \times \begin{Bmatrix} 1 & 1 & 2 \\ J_g & J_g & J_n \end{Bmatrix} \frac{f_{gn}^{(1)}}{(\Delta E_{gn})^2 - \omega^2},
\end{aligned}
\tag{5}
$$

with $f_{gn}^{(1)}$ being the dipole oscillator strength, and

$$
f_{gn}^{(1)} = \frac{2|\langle N_g J_g \| T_1 \| N_n J_n \rangle|^2 \Delta E_{gn}}{3(2J_g+1)},
\tag{6}
$$

where $\Delta E_{gn} = E_n - E_g$ is the transition energy between initial state $|N_g J_g\rangle$ and intermediate state $|N_n J_n\rangle$, and T_1 is the dipole transition operator.

QED corrections to polarizability and magic wavelength can be obtained by the perturbation theory using accurate energies and wave functions from NRCI calculations [38]. The general approach allowing an approximate evaluation of the QED corrections to the static dipole polarizability was formulated by Pachucki and Sapirstein [39]. Similarly, the formula of QED correction to the dynamic dipole polarizability has been derived in Refs. [25,40] as

$$
\begin{aligned}
\delta\alpha_1^{\text{QED}}(\omega) = 2\Bigg[& \sum_n \frac{\langle N_g L_g | T_1 | N_n L_n \rangle \langle N_n L_n | T_1 | N_g L_g \rangle \langle N_g L_g | \delta H_{\text{QED}} | N_g L_g \rangle (\Delta E_{gn}^2 + \omega^2)}{(\Delta E_{gn}^2 - \omega^2)^2} \\
& - 2\sum_{nm} \frac{\langle N_g L_g | T_1 | N_n L_n \rangle \langle N_n L_n | T_1 | N_m L_m \rangle \langle N_m L_m | \delta H_{\text{QED}} | N_g L_g \rangle \Delta E_{gn}}{(\Delta E_{gn}^2 - \omega^2) \Delta E_{gm}} \\
& - \sum_{nm} \frac{\langle N_g L_g | T_1 | N_n L_n \rangle \langle N_n L_n | \delta H_{\text{QED}} | N_m L_m \rangle \langle N_m L_m | T_1 | N_g L_g \rangle (\Delta E_{gn} \Delta E_{gm} + \omega^2)}{(\Delta E_{gn}^2 - \omega^2)(\Delta E_{gm}^2 - \omega^2)} \Bigg],
\end{aligned}
\tag{7}
$$

TABLE I. Comparison of present transition energies and oscillator strengths (both in a.u.) for the $2\,^1P \to n\,^1S/n\,^1D$ transitions of helium with Hylleraas results obtained by Drake and Morton [45,46]. The numbers in parentheses are numerical convergence uncertainties. The relativistic Hylleraas oscillator strengths of ^{4}He listed in the third column are obtained by adding the finite nuclear mass effects [45] to the relativistic oscillator strengths of $^\infty$He [46]. The nonrelativistic Hylleraas oscillator strengths of ^{4}He in the fifth column are obtained by multiplying a factor of $(m_0 + Z)/m_0$ to the Hylleraas results of ^{4}He [45].

	Relativistic values of ^{4}He		Nonrelativistic values of ^{4}He		Nonrelativistic values of $^\infty$He	
	RCI	Hylleraas [45,46]	NRCI	Hylleraas [45]	NRCI	Hylleraas [45]
$\Delta E_{2\,^1P \to n\,^1S/n\,^1D}$						
$2\,^1P \to 1\,^1S$	−0.779 74(1)	−0.779 754 214	−0.779 741(2)	−0.779 758 897	−0.779 863(2)	−0.779 881 290
$2\,^1P \to 2\,^1S$	−0.022 132 5(3)	−0.022 132 621	−0.022 133 2(1)	−0.022 132 934	−0.022 131 2(1)	−0.022 130 959
$2\,^1P \to 3\,^1S$	0.062 557 0(4)	0.062 558 064	0.062 555 5(1)	0.062 556 569	0.062 570 0(1)	0.062 571 096
$2\,^1P \to 4\,^1S$	0.090 238 4(5)	0.090 239 679	0.090 236 6(1)	0.090 237 834	0.090 255 1(1)	0.090 256 369
$2\,^1P \to 3\,^1D$	0.068 207 3(6)	0.068 208 662	0.068 205 3(1)	0.068 206 657	0.068 220 9(1)	0.068 222 353
$2\,^1P \to 4\,^1D$	0.092 544 8(5)	0.092 546 277	0.092 542 8(1)	0.092 544 223	0.092 561 9(1)	0.092 563 240
$2\,^1P \to 5\,^1D$	0.103 807(1)	0.103 808 782	0.103 805 3(1)	0.103 806 697	0.103 825 8(1)	0.103 827 250
$2\,^1P \to 6\,^1D$	0.109 924(1)	0.109 925 574	0.109 922 1(1)	0.109 923 471	0.109 943 5(1)	0.109 944 859
$f^{(1)}_{2\,^1P \to n\,^1S/n\,^1D}$						
$2\,^1P \to 1\,^1S$	−0.092 047(2)	−0.092 050	−0.092 048(2)	−0.092 051 3	−0.092 051(2)	−0.092 054 9
$2\,^1P \to 2\,^1S$	−0.125 533(2)	−0.125 53	−0.125 540(2)	−0.125 536 1	−0.125 484(2)	−0.125 480 1
$2\,^1P \to 3\,^1S$	0.048 511(2)	0.048 512	0.048 514(2)	0.048 512 4	0.048 492(2)	0.048 490 1
$2\,^1P \to 4\,^1S$	0.008 627(2)	0.008 626 8	0.008 627(2)	0.008 626 8	0.008 624(2)	0.008 623 4
$2\,^1P \to 3\,^1D$	0.710 14(4)	0.710 17	0.710 347(2)	0.710 331 5	0.710 179(2)	0.710 164 1
$2\,^1P \to 4\,^1D$	0.120 28(2)	0.120 27	0.120 281(2)	0.120 281 8	0.120 269(2)	0.120 270 4
$2\,^1P \to 5\,^1D$	0.043 257(6)	0.043 256	0.043 259(2)	0.043 259 5	0.043 257(2)	0.043 257 6
$2\,^1P \to 6\,^1D$	0.020 948(2)	0.020 947	0.020 948(4)	0.020 948 9	0.020 948(2)	0.020 948 5

where $|N_g L_g\rangle$ represents the nonrelativistic wave function of the initial state, $|N_n L_n\rangle$ and $|N_m L_m\rangle$ represent nonrelativistic wave functions of intermediate states, and the expansion for the QED operator, δH_{QED}, on the order α^3 is [41,42]

$$\delta H_{\mathrm{QED}}^{(3)} = \frac{4Z\alpha^3}{3} \left\{ \frac{19}{30} + \ln[(Z\alpha)^{-2}] - \ln\left(\frac{k_0}{Z^2}\right) \right\}$$
$$\times [\delta^3(r_1) + \delta^3(r_2)] + O(r_{12}), \qquad (8)$$

where $\ln k_0$ is the Bethe logarithm and $O(r_{12})$ represents the remaining term connected with r_{12}. In the present calculations, we use Bethe logarithms from Ref. [43] for the $2\,^3S_1$ and $2\,^1P_1$ states of ^{4}He.

III. STATIC POLARIZABILITIES

We use a complete set of configuration wave functions on an exponential grid [44] generated using B-splines constrained to a spherical cavity. A cavity radius of 200 a.u. is chosen to accommodate the initial state and the corresponding intermediate states and is suitable for obtaining the frequency-dependent polarizabilities for the $2\,^3S_1$ and $2\,^1P_1$ states in the range above 389 nm, which is the second resonance wavelength of the $2\,^3S_1$ state. The basis set consists of 40, 45, and 50 B splines for each value of the partial wave less than $\ell_{\max} = 10$.

The values of some selected transition energies and oscillator strengths are listed in Table I, and a detailed comparison between present B-spline calculations and Drake and Morton's Hylleraas calculations [45,46] is also made in Table I. The numerical convergence uncertainties of the present values are evaluated as the difference between our extrapolated value and the result under the largest basis set. For transition energies, the nonrelativistic Hylleraas energies of ^{4}He are obtained by adding the finite nuclear mass shifts to the $^\infty$He energies [45], and the relativistic Hylleraas energies of ^{4}He are converted from the ionization energies in MHz [45]. It is seen that our RCI and NRCI results of transition energies are all in general agreement with Hylleraas values [45].

For oscillator strengths, the relativistic Hylleraas oscillator strengths of ^{4}He are obtained by adding the finite nuclear mass effects [45] to the relativistic oscillator strengths of $^\infty$He [46], and the nonrelativistic Hylleraas oscillator strengths of ^{4}He listed in the fifth column of Table I are obtained by multiplying a factor of $(m_0 + Z)/m_0$ to the Hylleraas results of ^{4}He [45]. The oscillator strengths of our NRCI results are in good agreement with those obtained from Hylleraas calculations [45] except for the $2\,^1P \to 1\,^1S$, $2\,^1P \to 2\,^1S$, and $2\,^1P \to 3\,^1D$ transitions. Those due to electron-electron correlations for these low-lying singlet states are not well accounted for in the CI method. Therefore, in the subsequent calculations, in order to take fully into account electron-electron correlation effect, we replace our transition energies and oscillator strengths for the $2\,^1P \to (1, 2, 3)\,^1S$ and $2\,^1P \to (3, 4)\,^1D$ transitions with Hylleraas transition energies and oscillator strengths, and then the computational uncertainties of our polarizabilities and magic wavelengths include two parts: One is from the numerical convergence error and the other is from the insufficient consideration of correlation effect.

The α^3 QED contributions to energies of $2\,^3S_1$ and $2\,^1P_1$ states omitting the $O(r_{12})$ term of Eq. (8) are calculated to be 0.000 016 713 and 0.000 016 115 a.u., which are slightly larger by 0.018% and 0.043% comparing with Yerokhin and Pachucki's values of 0.000 016 710 and 0.000 016 108 a.u.

TABLE II. The static dipole polarizabilities (in a.u.) for the $2\,^1P_1$ state of helium. The numbers in parentheses are computational uncertainties.

Term	(RCI, ^{4}He)	(NRCI, ^{4}He)	(NRCI, $^\infty$He)	α^3 QED
$\alpha_1^S(0)$	$-59.619(6)$	$-59.959(6)$	$-60.022(7)$	$-0.006\,02(2)$
$\alpha_1^T(0)$	$223.59(2)$	$223.554(2)$	$223.511(2)$	$0.006\,11(2)$
$\alpha_1(0)(M=0)$	$-506.80(2)$	$-507.067(6)$	$-507.043(4)$	$-0.018\,2(2)$
$\alpha_1(0)(M=\pm1)$	$163.97(2)$	$163.60(2)$	$163.49(2)$	$0.000\,098(2)$

[41], respectively. This indicates that contribution from the $O(r_{12})$ term is at least three orders of magnitude smaller than the first term in Eq. (8). So, in the subsequent calculations, QED corrections from $O(r_{12})$ term will be neglected.

Static dipole polarizabilities for the $2\,^1P_1$ state of helium are given in Table II. For the scalar component of the $2\,^1P_1$ state of $^\infty$He, there are four figures consistent between the present NRCI result and Hylleraas value of $-60.028\,5140(2)$ a.u. [47]. Comparing the RCI and NRCI static polarizabilities of ^{4}He, we find that the relativistic correction is positive for the $2\,^1P_1$ state, which is different from the ground state [39,42] and the $2\,^3S_1$ metastable state [25].

Table II also shows the α^3 QED corrections to the static dipole polarizabilities for the $2\,^1P_1$ state. The fractional uncertainties are larger than the differences between QED corrections from the first term of Eq. (8) and the total α^3 corrections [41] to energies, which guarantees the reliability of present QED corrections to polarizabilities. When an atom is in the external electric field ε, the electric-field derivative of Bethe logarithm of $\partial_\varepsilon^2 lnk_0$ introduces about 0.6% of the α^3 QED correction (without $\partial_\varepsilon^2 lnk_0$) to the ground-state polarizability [24,48]. In previous calculations, the correction from $\partial_\varepsilon^2 lnk_0$ was evaluated by indicating 1% of the α^3 QED correction to the polarizability [25]. However, this correction can be neglected under the present computational uncertainties for polarizabilities.

IV. MAGIC WAVELENGTHS

The total dynamic polarizabilities for the $2\,^3S_1$ and $2\,^1P_1$ states depend upon their magnetic quantum numbers of M. Therefore, the magic wavelengths need to be determined separately for the cases with $M=0$ and $M=\pm1$ for the $2\,^3S_1 \rightarrow 2\,^1P_1$ transitions, owing to the presence of the tensor contribution to the total polarizabilites of the $2\,^3S_1$ and $2\,^1P_1$ states. The transitions of $2\,^3S_1(M=0) \rightarrow 2\,^1P_1(M=\pm1)$ and $2\,^3S_1(M=\pm1) \rightarrow 2\,^1P_1(M=\pm1)$ have the same number of magic wavelengths in the range above 389 nm, and magic wavelengths for these two transitions are the same under present computational accuracy. We plot the frequency-dependent polarizabilities in the range 390–540 nm for the $2\,^3S_1(M=\pm1)$ and $2\,^1P_1(M=\pm1)$ magnetic substates in Fig. 1. The positions of the resonances are indicated by vertical dashed lines with small arrows on top of the graph. There are five resonances ($2\,^1P_1 \rightarrow n\,^1D_2$, $n=4$–8) in this wavelength region, and five magic wavelengths for the $2\,^3S_1(M=\pm1) \rightarrow 2\,^1P_1(M=\pm1)$ transition which are all marked with arrows. In addition, there is no magic wavelength above 540 nm since there is no contribution from the $2\,^1P_1 - 2\,^1S_0$ and $2\,^1P_1 - 3\,^1S_0$ resonances, because $n\,^1S_0$ contributions to the scalar and tensor polarizabilities of the $2\,^1P_1(M=\pm1)$ state cancel each other out.

The other transitions of $2\,^3S_1(M=0) \rightarrow 2\,^1P_1(M=0)$ and $2\,^3S_1(M=\pm1) \rightarrow 2\,^1P_1(M=0)$ have the same number of magic wavelengths as well. Magic wavelengths and the corresponding polarizabilities for the transition final state of $2\,^1P_1(M=0)$ are given in Table III. In the present RCI calculations, except for the first magic wavelength at 1335 nm, magic wavelengths for the $2\,^3S_1(M=0) \rightarrow 2\,^1P_1(M=0)$ and $2\,^3S_1(M=\pm1) \rightarrow 2\,^1P_1(M=0)$ transitions are the same within the listed uncertainties, so only one set of magic wavelengths data is listed. While the dynamic polarizabilities at the corresponding magic wavelengths for these two transitions are slightly different, we list both sets of polarizability data to illustrate the differences from different magnetic substates. NRCI results of magic wavelengths and the corresponding dynamic polarizabilities for ^{4}He and $^\infty$He are given in the last four columns of Table III. By comparing the NRCI results of ^{4}He and $^\infty$He, we will extract the finite nuclear mass corrections to magic wavelengths and polarizabilities. The relativistic effects are extracted from the RCI results and the NRCI results of ^{4}He.

The first two longer magic wavelengths for the $2\,^3S_1(M=\pm1) \rightarrow 2\,^1P_1(M=0)$ transition are displayed in Fig. 2. Comparisons of the percentages of finite nuclear mass and relativistic contributions to magic wavelengths are shown graphically in Fig. 3. It is found that the line shape of the dynamic polarizabilities curve of $2\,^1P(M=0)$ near 1335-nm
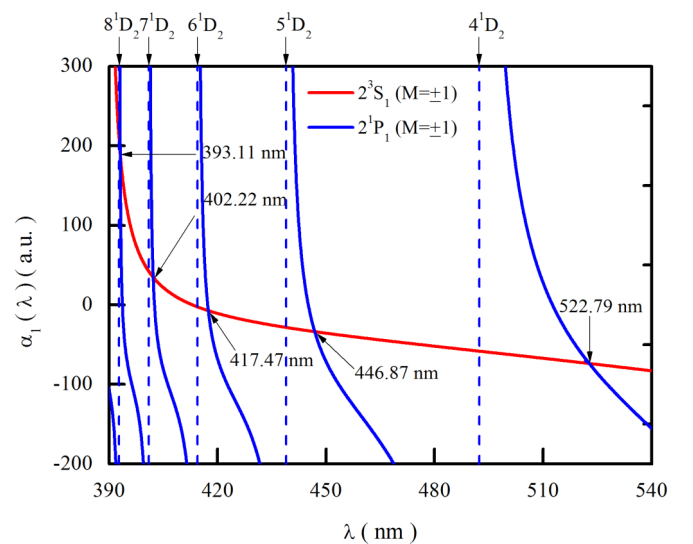

FIG. 1. The frequency-dependent polarizabilities for the $2\,^3S_1(M=\pm1)$ and $2\,^1P_1(M=\pm1)$ states of ^{4}He. The magic wavelengths are marked with arrows. The positions of the resonances are indicated by vertical dashed lines with small arrows on top of the graph.

TABLE III. Magic wavelengths (in nm) and the corresponding dynamic dipole polarizabilities (in a.u.) for the $2\,^3S_1 \to 2\,^1P_1(M=0)$ transition of helium. The numbers in parentheses are computational uncertainties.

	(RCI, ^{4}He) $2\,^3S_1(M=0/\pm 1) \to 2\,^1P_1$		(NRCI, ^{4}He) $2\,^3S \to 2\,^1P$		(NRCI, $^\infty$He) $2\,^3S \to 2\,^1P$	
No.	λ_m	$\alpha_1(\lambda_m)$	λ_m	$\alpha_1(\lambda_m)$	λ_m	$\alpha_1(\lambda_m)$
1	1335.486(4)/1335.523(5)	902.54(2)/902.59(2)	1335.85(2)	902.82(3)	1335.54(2)	901.81(3)
2	720.54(2)	−228.08(2)/−228.05(2)	720.56(1)	−227.93(2)	720.39(1)	−227.93(2)
3	527.90(2)	−76.527(4)/−76.518(4)	527.867(2)	−76.457(2)	527.765(2)	−76.467(2)
4	502.44(2)	−63.417(2)/−63.409(4)	502.448(2)	−63.371(2)	502.346(2)	−63.381(2)
5	449.28(2)	−35.265(4)/−35.258(4)	449.271(2)	−35.208(2)	449.184(2)	−35.229(2)
6	442.665(4)	−31.027(4)/−31.020(4)	442.672(2)	−30.976(2)	442.585(2)	−30.998(2)
7	418.872(4)	−9.280(6/−9.270(6)	418.873(2)	−9.192(2)	418.792(2)	−9.228(2)
8	416.273(4)	−5.498(8)/−5.49(2)	416.279(2)	−5.411(2)	416.199(2)	−5.448(2)
9	403.172(4)	29.73(2)/29.75(2)	403.176(2)	29.942(2)	403.098(2)	29.894(4)
10	401.958(4)	36.15(2)/36.17(2)	401.964(2)	36.378(2)	401.886(2)	36.330(2)
11	393.863(4)	155.3(2)/155.4(2)	393.868(2)	156.50(2)	393.792(2)	156.61(2)
12	393.138(4)	188.0(2)/188.1(2)	393.142(2)	189.69(4)	393.067(2)	189.90(4)

magic wavelength is different from that near other magic wavelengths shown in Figs. 1 and 2. Moreover, it indicates that the percentages of finite nuclear mass and relativistic corrections to the 1335-nm magic wavelength are larger than those of other magic wavelengths from Fig. 3.

We discuss the finite nuclear mass, relativistic, and QED effects on the 1335-nm magic wavelength for the $2\,^3S_1(M = \pm 1) \to 2\,^1P_1(M = 0)$ transition of ^{4}He (the $2\,^3S_1$ state with the $M=1$ magnetic substate is the magnetically trapped state [49]) in detail. Table IV gives the breakdown of different contributions to the 1335-nm magic wavelength and to the corresponding dynamic dipole polarizability. The finite nuclear mass corrections are obtained by comparing the NRCI results of ^{4}He and $^\infty$He, and the relativistic effects are extracted from the RCI results and the NRCI results of ^{4}He,

which are all listed in the third line of Table III. The leading QED corrections given in Table IV are obtained by the perturbation method. The QED contributions of 0.028(2) nm and 0.009 6(2) a.u. are added to the RCI values of 1335.523(5) nm and 902.59(2) a.u., which give 1335.55(2) nm for the magic wavelength and 902.60(2) a.u. for the dynamic polarizability, respectively. The α^4 order QED effects on the 1335-nm magic wavelength and the corresponding dynamic polarizability are estimated as we have done for the 413-nm tune-out wavelength [25], they are respectively 0.000 49 nm and 0.000 17 a.u., which can be neglected in the present computational uncertainties.

For the 1335-nm magic wavelength, from Table IV, we obtain that the finite nuclear mass, relativistic, and QED effects on the 1335.55(2)-nm magic wavelength are respectively 232, 247, and 21 ppm. Moreover, the finite nuclear mass, relativistic, and QED corrections calculated here cancel out almost completely under the present computational
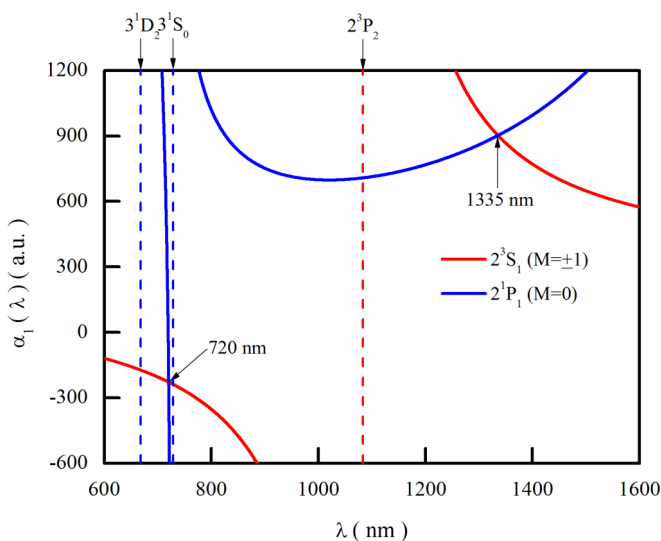

FIG. 2. The frequency-dependent polarizabilities for the $2\,^3S_1(M = \pm 1)$ and $2\,^1P_1(M = 0)$ states of ^{4}He. The magic wavelengths are marked with arrows. The positions of the resonances are indicated by vertical dashed lines with small arrows on top of the graph.
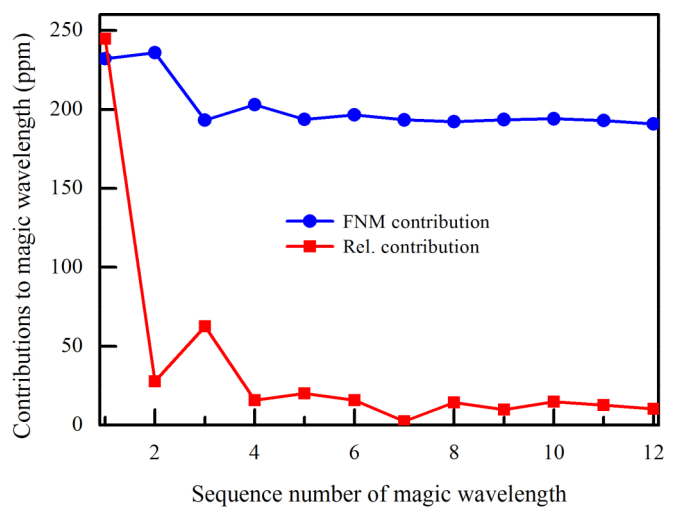

FIG. 3. Comparisons of the finite nuclear mass (FNM) and relativistic (Rel.) contributions to each magic wavelength for the $2\,^3S_1(M = \pm 1) \to 2\,^1P_1(M = 0)$ transition of ^{4}He.

TABLE IV. Contributions to the 1335-nm magic wavelength (in nm) for the $2\,^3S_1(M=\pm1) \rightarrow 2\,^1P_1(M=0)$ transition and the dynamic dipole polarizability (in a.u.) at the 1335-nm magic wavelength of ^{4}He. FNM and Rel. represent the finite nuclear mass and relativistic corrections, the present RCI results include the FNM and Rel. corrections, and the leading QED corrections are obtained by perturbation calculations. The numbers in parentheses are computational uncertainties.

Contributions	λ_m	$\alpha_1(\lambda_m)$
FNM	0.31(2)	1.01(3)
Rel.	−0.33(2)	−0.23(3)
RCI	1335.523(5)	902.59(2)
QED	0.028(2)	0.009 6(2)
Total	1335.55(2)	902.60(2)

uncertainties. Thus, the final result of 1335.55(2) nm of ^{4}He is slightly discrepant from the NRCI result of 1335.545(2) nm for $^\infty$He.

QED contribution to the 1335-nm magic wavelength is comparable to the ground and the $2\,^3S_1$ metastable state static polarizabilities ($\approx$22 ppm) [24,25], but high-precision measurement of magic wavelength is more feasible than that of polarizability. Moreover, while magic wavelengths and tune-out wavelengths both permit measurements of high precision, QED sensitivity of the 1335-nm magic wavelength is almost twice that of the 413-nm tune-out wavelength ($\approx$10 ppm) [25]. It is concluded that measurement of the 1335.55(2)-nm magic wavelength for the $2\,^3S_1(M=\pm1) \rightarrow 2\,^1P_1(M=0)$ transition of ^{4}He would provide another nonenergy test of fundamental atomic structure theory, which might be comparable to or better than measurement of the 413-nm tune-out wavelength [25,27,28].

The magic wavelength for the $2\,^3S_1(M=\pm1) \rightarrow 2\,^1P_1(M=0)$ transition of ^{4}He, present computed value of 1335.55(2) nm is equivalent to 224 471(4) GHz, which indicates that, if measured, a magic frequency with an accuracy of better than GHz will reflect the leading QED correction. As mentioned in the introduction, magic wavelengths measured in most of current experiments have

been at the level of MHz, so we reasonably inferred that higher order QED effects may be tested provided that the 224 471-GHz magic frequency can be measured with a precision of MHz and higher accuracy theoretical calculations can be achieved as well.

V. CONCLUSION

We have calculated the frequency-dependent dipole polarizabilities for the $2\,^1P_1$ state and determined a series of magic wavelengths for the $2\,^3S_1 \rightarrow 2\,^1P_1$ forbidden transition of helium. Using a perturbation method, the leading QED corrections to polarizabilities and magic wavelengths are taken into account. In the present RCI calculations, we obtain the static scalar and tensor dipole polarizabilities of −59.619(6) and 223.59(2) a.u. for the $2\,^1P_1$ state, and the corresponding leading QED corrections are −0.006 02(2) and 0.006 11(2) a.u.. The finite nuclear mass, relativistic, and QED corrections to the 1335.55(2)-nm magic wavelength for the $2\,^3S_1(M=\pm1) \rightarrow 2\,^1P_1(M=0)$ transition are respectively 232, 247, and 21 ppm, and a precision of better than 0.01 nm in the magic wavelength would reflect the atomic structure information related to QED effects. Since the 1335-nm magic wavelength is sensitive to the finite nuclear mass, relativistic, and QED effects, and moreover the measurement of magic wavelengths with high precision is feasible, we suggest that the 1335-nm magic wavelength would probably serve as one of atomic structure theory probes.

[1] W. E. Lamb and R. C. Retherford, Phys. Rev. **72**, 241 (1947).

[2] S. Sturm, F. Köhler, J. Zatorski, A. Wagner, Z. Harman, G. Werth, W. Quint, C. H. Keitel, and K. Blaum, Nature (London) **506**, 467 (2014).

[3] M. G. Kozlov, M. S. Safronova, J. R. Crespo López-Urrutia, and P. O. Schmidt, Rev. Mod. Phys. **90**, 045005 (2018).

[4] N. Bezginov, T. Valdez, M. Horbatsch, A. Marsman, A. C. Vutha, and E. A. Hessels, Science **365**, 1007 (2019).

[5] K. Pachucki, V. Patkóš, and V. A. Yerokhin, Phys. Rev. A **95**, 062510 (2017).

[6] V. Patkóš, V. A. Yerokhin, and K. Pachucki, Phys. Rev. A **95**, 012508 (2017).

[7] V. Patkóš, V. A. Yerokhin, and K. Pachucki, Phys. Rev. A **94**, 052508 (2016).

[8] S. D. Bergeson, A. Balakrishnan, K. G. H. Baldwin, T. B. Lucatorto, J. P. Marangos, T. J. McIlrath, T. R. O'Brian, S. L. Rolston, C. J. Sansonetti, J. Wen *et al.*, Phys. Rev. Lett. **80**, 3475 (1998).

[9] D. Z. Kandula, C. Gohle, T. J. Pinkert, W. Ubachs, and K. S. E. Eikema, Phys. Rev. Lett. **105**, 063001 (2010).

[10] D. Z. Kandula, C. Gohle, T. J. Pinkert, W. Ubachs, and K. S. E. Eikema, Phys. Rev. A **84**, 062512 (2011).

[11] M. Smiciklas and D. Shiner, Phys. Rev. Lett. **105**, 123001 (2010).

[12] X. Zheng, Y. R. Sun, J. J. Chen, W. Jiang, K. Pachucki, and S. M. Hu, Phys. Rev. Lett. **119**, 263002 (2017).

[13] K. Kato, T. D. G. Skinner, and E. A. Hessels, Phys. Rev. Lett. **121**, 143002 (2018).

[14] K. Pachucki and V. A. Yerokhin, J. Phys. Conf. Ser. **264**, 012007 (2011).

[15] D. Shiner, R. Dixson, and V. Vedantham, Phys. Rev. Lett. **74**, 3553 (1995).

[16] P. C. Pastor, G. Giusfredi, P. De Natale, G. Hagel, C. de Mauro, and M. Inguscio, Phys. Rev. Lett. **92**, 023001 (2004).

[17] P. C. Pastor, L. Consolino, G. Giusfredi, P. De Natale, M. Inguscio, V. A. Yerokhin, and K. Pachucki, Phys. Rev. Lett. **108**, 143001 (2012).

[18] K. A. H. van Leeuwen and W. Vassen, EPL **76**, 409 (2006).

[19] R. van Rooij, J. S. Borbely, J. Simonet, M. D. Hoogerland, K. S. E. Eikema, R. A. Rozendaal, and W. Vassen, Science **333**, 196 (2011).

[20] R. J. Rengelink, Y. van der Werf, R. P. M. J. W. Notermans, R. Jannin, K. S. E. Eikema, M. D. Hoogerland, and W. Vassen, Nat. Phys. **14**, 1132 (2018).

[21] V. Patkóš, V. A. Yerokhin, and K. Pachucki, Phys. Rev. A **101**, 062516 (2020).

[22] G. Łach and K. Pachucki, Phys. Rev. A **64**, 042510 (2001).

[23] C. Gaiser and B. Fellmuth, Phys. Rev. Lett. **120**, 123203 (2018).

[24] M. Puchalski, K. Szalewicz, M. Lesiuk, and B. Jeziorski, Phys. Rev. A **101**, 022505 (2020).

[25] Y. H. Zhang, F. F. Wu, P. P. Zhang, L. Y. Tang, J. Y. Zhang, K. G. H. Baldwin, and T. Y. Shi, Phys. Rev. A **99**, 040502(R) (2019).

[26] J. Mitroy and L. Y. Tang, Phys. Rev. A **88**, 052515 (2013).

[27] G. W. F. Drake, J. G. Manalo, P. P. Zhang, and K. G. H. Baldwin, Hyperfine Interact. **240**, 31 (2019).

[28] B. M. Henson, R. I. Khakimov, R. G. Dall, K. G. H. Baldwin, L. Y. Tang, and A. G. Truscott, Phys. Rev. Lett. **115**, 043004 (2015).

[29] I. Ushijima, M. Takamoto, and H. Katori, Phys. Rev. Lett. **121**, 263202 (2018).

[30] A. Derevianko and H. Katori, Rev. Mod. Phys. **83**, 331 (2011).

[31] P. J. Mohr, B. N. Taylor, and D. B. Newell, Rev. Mod. Phys. **84**, 1527 (2012).

[32] I. I. Tupitsyn, V. M. Shabaev, J. R. Crespo López-Urrutia, I. Draganić, R. S. Orts, and J. Ullrich, Phys. Rev. A **68**, 022511 (2003).

[33] V. M. Shabaev, Theor. Math. Phys. **63**, 588 (1985) [Sov. J. Nucl. Phys. **47**, 69 (1988)].

[34] C. W. Palmer, J. Phys. B **20**, 5987 (1987).

[35] W. R. Johnson, S. A. Blundell, and J. Sapirstein, Phys. Rev. A **37**, 307 (1988).

[36] L. Y. Tang, Y. H. Zhang, X. Z. Zhang, J. Jiang, and J. Mitroy, Phys. Rev. A **86**, 012505 (2012).

[37] J. Mitroy, M. S. Safronova, and C. W. Clark, J. Phys. B **43**, 202001 (2010).

[38] Y. H. Zhang, L. Y. Tang, X. Z. Zhang, and T. Y. Shi, Phys. Rev. A **93**, 052516 (2016).

[39] K. Pachucki and J. Sapirstein, Phys. Rev. A **63**, 012504 (2000).

[40] F. F. Wu, S. J. Yang, Y. H. Zhang, J. Y. Zhang, H. X. Qiao, T. Y. Shi, and L. Y. Tang, Phys. Rev. A **98**, 040501(R) (2018).

[41] V. A. Yerokhin and K. Pachucki, Phys. Rev. A **81**, 022507 (2010).

[42] M. Puchalski, K. Piszczatowski, J. Komasa, B. Jeziorski, and K. Szalewicz, Phys. Rev. A **93**, 032515 (2016).

[43] V. I. Korobov, Phys. Rev. A **100**, 012517 (2019).

[44] H. Bachau, E. Cormier, P. Decleva, J. E. Hansen, and F. Martín, Rep. Prog. Phys. **64**, 1815 (2001).

[45] G. W. F. Drake, *Handbook of Atomic, Molecular, and Optical Physics* (Springer, New York, 2006).

[46] G. W. F. Drake and D. C. Morton, Astrophys. J. Suppl. Ser. **170**, 251 (2007).

[47] Z. C. Yan, Phys. Rev. A **62**, 052502 (2000).

[48] G. Łach, B. Jeziorski, and K. Szalewicz, Phys. Rev. Lett. **92**, 233001 (2004).

[49] R. Dall and A. Truscott, Opt. Commun. **270**, 255 (2007).